1   **Subduction megathrust creep governed by pressure solution and**

2   **frictional-viscous flow**

3   Åke Fagereng[1,2,*] & Sabine A. M. den Hartog[3,4]

4   [1]*School of Earth & Ocean Sciences, Cardiff University, Cardiff, CF10 3AT, United*

5   *Kingdom.*

6   [2]*Department of Geological Sciences, University of Cape Town, Private Bag X3,*

7   *Rondebosch 7701, South Africa.*

8   [3]*HPT Laboratory, Department of Earth Sciences, Utrecht University, Utrecht, The*

9   *Netherlands.*

10   [4]*Now at: Rock Deformation Laboratory, School of Environmental Sciences, University*

11   *of Liverpool, Liverpool, United Kingdom*

12   *Corresponding author: FagerengA@cardiff.ac.uk

13   **Subduction megathrust slip speeds range from slow creep at plate convergence**

14   **rates (centimetres per year) to seismic slip rates (metres per second) in the largest**

15   **earthquakes on Earth. The deformation mechanisms controlling whether fast slip**

16   **or slow creep occurs, however, remain unclear. Here, we present evidence that**

17   **pressure solution creep - fluid-assisted, stress-driven mass transfer - is an**

18   **important deformation mechanism in megathrust faults. We quantify megathrust**

19   **strength using a laboratory-constrained microphysical model for fault friction,**

20   **involving viscous pressure solution and frictional sliding. We find that at plate-**

21   **boundary deformation rates, aseismic, frictional-viscous flow is the preferred**

22 **deformation mechanism at temperatures above 100 ˚C. The model thus predicts**

23 **aseismic creep at temperatures much cooler than the onset of crystal plasticity,**

24 **unless a boundary condition changes. Within this model framework, earthquakes**

25 **may nucleate when a local increase in strain rate triggers velocity-weakening slip,**

26 **and we speculate that slip area and event magnitude increase with increasing**

27 **spacing of strong, topographically derived irregularities in the subduction**

28 **interface.**

29   Understanding why some megathrust segments accommodate displacement by

30 earthquake slip versus aseismic creep is a major challenge. Geophysically observed

31 variation in seismic style along active subduction megathrusts, involving a continuum

32 of slip speeds from plate boundary creep rates to earthquake slip[1], arises from processes

33 within a fault zone in subducting sediments on top of potentially rugged ocean floor[2-6].

34 Dominantly creeping margins are characterised by low seismic coupling coefficients -

35 the observed seismic moment release rate over that required by plate motion vectors -

36 and lack of earthquake moment magnitudes $\geq$ 8.0 (Supplementary Figure S1)[7,8]. Thus,

37 some margins produce small to medium magnitude earthquakes, but the total moment of

38 these earthquakes is insufficient to explain total geodetically observed displacement,

39 and they must therefore be accompanied by aseismic creep[9].

40   The megathrust interface is commonly inferred as seismogenic to a depth where

41 temperature exceeds the 350˚C required for crystal plasticity in quartz, or to the

42 intersection with the hanging wall Moho, whichever is shallower[10]. However, geodetic

43 inversions[8,11-14] reveal aseismic creep shallower than both the 350˚C isotherm and the

44 hanging wall Moho. The question thus arises: how do some megathrust segments, such

45   as north Hikurangi[11], the southern Japan Trench[12], southern New Hebrides[13], southern

46   Kermadec Arc[13], and the Manila Trench[14] accommodate detectable displacement by

47   aseismic creep in addition to moderate size earthquakes, both originating at a similar

48   depth range? This observation requires average creep rates of centimetres per year at

49   temperatures less than 350°C. Identifying the associated creep mechanism is critical for

50   recognising where megathrust displacement can occur without great earthquakes, and

51   by contrast, interpret where great earthquakes may occur.

52   **The mechanism of creep at seismogenic zone conditions**

53   Tectonic mélanges comprising sheared trench-fill and ocean floor sediments have

54   been interpreted as megathrust fault rocks (Fig. 1a)[3-6,15]. Deformation structures

55   developed at seismogenic pressure-temperature ($P - T$) conditions include both

56   discontinuities, such as faults and tensile fractures, and continuous structures such as

57   folds, boudins and foliations. One possible interpretation is that faults and associated

58   fractures represent seismic deformation styles, whereas continuous features characterise

59   slower, distributed, aseismic mechanisms recorded as creep[5,6,15]. In this interpretation,

60   the mechanism accommodating deformation in continuous structures is responsible for

61   aseismic creep.

62   In exhumed subduction thrusts, cleavage defined by fine-grained phyllosilicates

63   wraps around rigid quartz clasts (Fig. 1b). Comparable microstructures are reported in

64   borehole samples from the creeping segment of the continental San Andreas transform

65   fault[16,17]. Mass balance calculations on San Andreas samples indicate pressure solution,

66   involving fluid-assisted, stress-driven mass transfer, as the cleavage-forming process[16].

67   If empirical rates can be extrapolated, pressure solution is fast enough to account for

68   aseismic sliding[16,18].

69   Pressure solution is also widely inferred as the dominant cleavage-forming

70   process in mudrocks and phyllites sampled from exhumed subduction thrusts[6,19-21]. As

71   an example, we consider a sample representative of sheared, cleaved mudstone from an

72   inferred exhumed megathrust in the Chrystalls Beach Complex, New Zealand[21](Fig. 1a-

73   e), where cleavage defined by illite-muscovite developed at $T < 300˚C$ (ref. *22*). In this

74   sample, cleavage seams are depleted in Si and enriched in Al (Fig. 1c; Supplementary

75   Figure 2). If cleavage develops by pressure solution, more soluble elements, such as Si,

76   are dissolved, whereas less soluble elements, such as Al, are retained. Thus, the

77   observations in the Chrystalls Beach sample are consistent with cleavage formation by

78   pressure solution. Stress shadows around quartz clasts lack evidence for opening of pore

79   space (Fig. 1d), and are sites of local silica enrichment (Fig. 1e). In addition to

80   formation of phyllosilicate cleavage, mass-transfer processes are therefore illustrated by

81   silica enrichment and clast elongation through mineral growth in pressure shadows (Fig.

82   1d,e).

83   **Microphysical model for fault gouge strength**

84   The observations on exhumed megathrust rocks indicate that one of the

85   microscopic processes that controls macroscopic frictional behaviour is viscous pressure

86   solution. Indeed, microphysical modelling studies have shown that experimental

87   observations on shear deformation at low strain rates in rocks comprising rigid clasts in

88   a phyllosilicate matrix can be explained by *frictional-viscous flow*: frictional sliding

89   along cleavage planes coupled to viscous (time-dependent) pressure solution of

90   intervening rigid clasts[23,24,25]. The microstructures reported in these experimental studies

91   are essentially identical to those seen in samples from the exhumed Chrystalls Beach

92   Complex (Fig. 1b-e). Frictional-viscous flow is restricted to low strain-rates (and/or

93   high T); at higher strain rates (or lower T), slip is activated on anastomosing

94   phyllosilicates, and microphysical models predict an importance of compaction by

95   pressure solution[24,25]. Here, we use the model by Den Hartog and Spiers[25], coupled to

96   analytical thermal gradients[26](Methods), to predict megathrust shear strength. This

97   microphysical model is based on friction experiments performed on materials and at

98   conditions representative for subduction megathrusts. Following this model, we assume

99   a matrix-supported megathrust shear zone where frictional sliding occurs on aligned

100   phyllosilicates, accommodated by pressure solution shear of intervening quartz grains or

101   dilatation (Fig. 1f). In this model, the relation between shear strain rate and shear stress

102   is derived by considering stress balances at the microscale for a unit cell defined in Fig.

103   1f. The megathrust shear strain rate ($\dot{\gamma}$) is related to the slip velocity (V) assuming strain

104   is distributed through a shear zone thickness (w) and therefore $\dot{\gamma} = V/w$.

105   Each unit cell consists of quartz clasts, which are uniformly distributed such that

106   horizontal rows overlap, and phyllosilicate foliations that are on average parallel to the

107   shear plane, but locally curve around rigid clasts (ref. *25*; Fig. 1f; Supplementary Figure

108   3), resembling the natural microstructure (Fig. 1b). Slip along foliation is assumed to be

109   a frictional process governed by the frictional resistance of phyllosilicates, which varies

110   with temperature and normal stress according to experimental data for illite and

111   muscovite[27-31](Methods). Depending on the conditions (e.g. slip velocity, temperature,

112   normal stress), the frictional resistance predicted by the model either decreases

113   (velocity-weakening) or increases (velocity-strengthening) as slip accelerates. Whereas

114   velocity-weakening behaviour is potentially unstable, and can promote fast earthquake

115   slip, velocity-strengthening behaviour is inferred to lead to stable sliding, recorded as

116   aseismic creep[32-34]. In the microphysical model used here[25], velocity-strengthening flow

117   occurs when easy shear of quartz clasts by thermally activated pressure solution, in

118   series with rate-independent slip on planar phyllosilicates, leads to non-dilatant

119   deformation (frictional-viscous flow). Velocity-weakening slip occurs when difficult

120   pressure solution shear of quartz results in increased shear stress and slip is activated on

121   curved phyllosilicate cleavages. This slip along curved foliation results in dilatation at

122   the clast-matrix interface under extension (Fig. 1f), which at steady state is balanced by

123   compaction via pressure solution.

124   **Application of flow law to natural subduction zones**

125   We apply boundary conditions appropriate for the northern Hikurangi margin, a

126   megathrust shown to deform predominantly by aseismic creep, at least over the last few

127   decades[11]. Pore fluid factors ($\lambda = P_f/\sigma_v$, where P_f is pore fluid pressure and σ_v is vertical

128   stress) of 0.8 and 0.95 are imposed to test variations between moderate and high fluid

129   pressure conditions. We distribute a steady creep rate of 40 mm yr^{-1} over a 1 - 100 m

130   thick subduction thrust shear zone, a range representing strain rates from 10^{-11} to 10^{-9} s^{-}

131   ^{1}, and a range in deforming thickness typical of exhumed mélanges and drilled

132   subduction megathrusts[15]. Quartz grain size varies from 10 to 100 μm, based on Fig. 1b-

133   e. All model parameters are listed in Supplementary Table S1.

134   The frictional-viscous flow strength of quartz-phyllosilicate mixtures as a function

135   of depth is compared to frictional strengths of mono-mineralic quartz and illite-

136   muscovite faults (Fig. 2a,b). At all considered conditions, frictional sliding in quartz

137   requires higher shear stress than any slip mechanism in phyllosilicates or quartz-

138   phyllosilicate mixtures; we therefore note that frictional sliding in quartz is an unlikely

139   deformation mechanism in phyllosilicate-rich megathrust shear zones. For both high

140   and moderate fluid overpressure, there is a depth below which frictional-viscous flow

141   requires a lower shear stress than that required for frictional sliding in mono-mineralic

142   phyllosilicate fault gouges (Fig. 2a,b). For deforming zones of 100 m thickness,

143   frictional viscous flow becomes favourable at 8 – 10 km depth in moderate fluid

144   pressure conditions (Fig. 2a), and at 12 – 16 km depth under high fluid pressure (Fig.

145   2b). In both cases, frictional-viscous flow becomes favourable at $T \geq 100 \pm 20$ ºC (Fig.

146   2c), where the corresponding shear stress, τ, is ≤ 10 MPa at high fluid pressure, and $\leq$

147   20 MPa at moderate fluid pressure (Fig. 2a,b). For a 1 m thick deforming zone, higher

148   strain rates make frictional-viscous flow less favourable; at high fluid pressure,

149   frictional sliding of phyllosilicates remains favourable until a depth of ~ 26 km ($T < 200$

150   ˚C, $\tau < 20$ MPa), whereas at lower fluid pressures, frictional sliding also requires higher

151   stresses and frictional-viscous flow becomes favourable from 16 km depth ($T < 150$ ˚C,

152     $\tau \sim 40$ MPa).

153   Calculated temperatures define low thermal gradients, partly because very low

154   stresses reduce temperatures relative to models with Byerlee friction (Fig. 2c). In our

155   warmest model, where $\lambda = 0.8$, shear zone width is 1 m, and quartz grain size 100 μm,

156   shear heating makes up approximately 30 % of the heat budget; for the coldest model,

157   with $\lambda = 0.95$, shear zone width of 100 m, and quartz grain size 10 μm, less than 10 %

158   of the heat budget is contributed by shear heating. Hikurangi is also a cool margin in the

159   global spectrum of subduction zone thermal models, where model temperatures[35]

160   compare to Fig. 2c. Compared to a recent numerical model[36], calculations here with $\lambda =$

161   0.8 are cooler at depths below ~ 10 km, whereas $\lambda = 0.95$ gives consistently lower

162   temperatures.

163   Aseismic frictional-viscous flow is the predicted deformation style at $T \geq 100$ ˚C,

164   when average plate boundary shear strain rates are accommodated in a hundreds of

165   metres thick shear zone (Fig. 2a,b). Generation of run-away earthquake slip requires a

166   change in these boundary conditions. This is because, at low strain rates, pressure

167   solution of quartz clasts accommodates local finite strain around the rigid clasts created

168   by slip on surrounding, planar phyllosilicate cleavages (Figs. 1d,e, 3a,b)[25]. At higher

169   strain rate, pressure solution requires greater driving stress, bulk fault zone strength

170   increases, and eventually dilatant, velocity-weakening behaviour occurs, allowing

171   potentially unstable slip[25] (Fig. 3a,b). At each depth increment in Fig. 2, we calculate

172   the friction coefficient as a function of strain rate, as shown for a depth of 30 km in Fig

173   3b. The strain rate required for a change from velocity-strengthening to velocity-

174   weakening behaviour increases with depth (Fig. 3c). At depths greater than 15 km,

175   where frictional-viscous flow generally becomes favourable (Fig. 2), velocity-

176   strengthening behaviour occurs at strain rates slower than 10^{-12} s^{-1} and shear zone

177   widths greater than tens of metres at 40 mm yr^{-1} slip rates (Fig. 3c). At a depth of 30

178   km, where frictional-viscous flow is preferred for all our considered conditions with a

179   plate boundary slip rate (Fig. 2a,b), the shear strain rates required for velocity-

180   weakening behaviour range from 10^{-9} to 10^{-4} s^{-1} (Fig. 3b,c).

181   At shallow depths, although commonly interpreted as a velocity-strengthening

182   region[10,34], potentially seismic slip is predicted at strain rates as low as 10^{-12} s^{-1} at 5 km

183   depth, and 10^{-16} s^{-1} at the surface (Fig. 3c). This is because shear deformation by

184   pressure solution of quartz is difficult at low temperature, yielding dilatant behaviour.

185   At greater depths, where $T \geq 100 \pm 20$ ºC, low strain rate frictional-viscous flow is the

186   predicted deformation mechanisms (Fig. 2), because a high quartz solubility yields

187   efficient dissolution and re-precipitation at this temperature (Ref. *37*, Supplementary

188   Figure 4). This potential change in deformation mechanism is reflected in exhumed

189   accretionary prisms, where mélange deformation at $T < 100$ ˚C is dominated by

190   distributed cataclasis, whereas a pressure solution cleavage and localised slip surfaces

191   are prevalent in rocks deformed at $T > 150$˚C (Refs. *6,21,38,39*). In central and northern

192   Hikurangi, the margin we used for our thermal calculations, it is uncertain whether a

193   near-surface velocity-strengthening zone and updip limit of seismicity is present, as

194   slow slip events may propagate to the trench[40]; the downdip limit of the interseismically

195   locked zone is here at less than 10 km depth[11]. This downdip limit of the locked zone is

196   in agreement with the onset of velocity-strengthening frictional-viscous flow at 10 km

197   depth and $T \leq 100$˚C, in a margin of moderate fluid overpressure and distributed shear

198   (Fig. 2a,c).

199   Following Den Hartog and Spiers[25], we conclude that frictional-viscous flow

200   involving pressure solution is a viable mechanism of velocity-strengthening, stable

201   creep. We consider the recently discovered phenomenon of slow slip along subduction

202   megathrusts[41,42], defined as geodetically observed displacement that is faster than plate

203   convergence rates but too slow to generate seismic waves, as a form of unstable slip[43].

204   Shallow slow slip, as observed near the trench in northern Hikurangi[40], may therefore be

205   a manifestation of unstable, dilatant shear at $T < 100°C$ (the 'potentially seismic slip' in

206   Fig. 3c). Deeper slow slip events occurring down-dip of the locked zone and at depths $\geq$

207   30 km, such as in Cascadia, are either independent of, or possibly load, the seismogenic

208   region[44]. The application of the microphysical model predicts velocity-strengthening

209   behaviour at such depths; thus, as for earthquakes, slow slip faster than steady-state

210   plate convergence rates requires a local change in conditions, possibilities of which we

211   discuss in the next section. Under the local triggering conditions, slow slip likely

212   reflects competition between deformation modes within a heterogeneous fault zone[45],

213   but may be an expression of either localised frictional sliding or distributed shearing

214   flow; differentiating between these basic geometries requires currently missing

215   knowledge of the deforming thickness during slow slip events.

216   **Relating creep to subduction of rugged vs. smooth slab topography**

217   Large earthquakes ($M_w \geq 8.0$) have been associated with subduction of smooth sea

218   floor, because a lack of barriers to slip – such as local topography, seamounts, and

219   horst-and-graben structures – allows for large rupture areas[2,46]. By comparison,

220   subduction of rugged ocean floor has been suggested to lead to smaller earthquakes

221   because rupture areas are geometrically constrained[2,12,36]. We therefore consider the

222   implications of the model results for two end-member subducting plates, with (i)

223   smooth and (ii) rugged topography[2,36,46].

224   (i) Smooth subducting slabs lack geometrical barriers to rupture propagation and

225   the fault zone has similar thickness and strain rate at all depths (Fig. 4a). However,

226   small-scale heterogeneities may locally elevate strain rates, causing velocity-weakening

10

227 behaviour (Fig. 3b,c), and triggering rupture propagation over a large area without

228 hindrance by large-scale barriers[4]. (ii) Rugged subducting ocean floor also deforms

229 predominantly via creep by frictional-viscous flow, and small-scale heterogeneities may

230 again lead to local velocity-weakening behaviour. However, in this case, strong,

231 topographically derived irregularities on the interface create barriers to earthquake

232 propagation, constraining earthquakes to smaller slip areas and therefore moderate

233 magnitudes (Fig. 4b). At and around such barriers, local brittle deformation occurs to

234 accommodate subduction of the topographic feature[2,12]. Extrapolating from continental

235 strike slip faults[47], we suggest that geometrical barriers - such as deformed, subducting

236 seamounts - that result in a discontinuity of potential slip surfaces by more than ~ 4 km,

237 are likely to arrest rupture propagation. Moreover, because of numerous stress and

238 strain-rate peaks, megathrusts associated with rugged subducting topography may

239 appear strong in stress calculations from heat flow measurements[36] or Coulomb wedge

240 mechanics[48], relative to fault segments where smooth subducting slabs allow large slip

241 areas on a through-going weak surface or a system of anastomosing slip surfaces. A

242 caveat to this broad, end-member interpretation is that subducting topography and

243 megathrust structure may evolve with depth. For example, subducting seamounts may

244 be progressively destroyed if they are indeed areas of increased brittle deformation[2], and

245 the microscale geometry within the fault zone can change through development of

246 through-going fault surfaces, mineral precipitation and reactions, and evolving grain

247 shapes and sizes, through progressive deformation, metamorphism and fluid flow[49]. As

248 such, the subduction thrust is a dynamic structure, displacing a footwall with inherently

249 complex geometry, and accurate predictions require high-resolution subsurface data.

250   In summary, our model offers an explanation for why megathrusts creep in some

251   places, and slip seismically in others. It implies that creep by frictional-viscous flow is

252   the preferred deformation mechanism of most if not all subduction thrust interfaces,

253   below some depth determined by thermal structure, strain rate, and fluid pressure (Figs.

254   2,3; Supplementary Figure 4). However, earthquakes may nucleate at local

255   heterogeneities where the behaviour is velocity-weakening[50]. Slip area and earthquake

256   magnitude should then depend on the spacing of strong, topographically derived

257   irregularities in the subduction interface, with giant earthquakes requiring this spacing

258   to be large.

259

260   **References**

261   1. Peng, Z. & Gomberg, J. An integrated perspective of the continuum between

262   earthquakes and slow slip phenomena. *Nat. Geosci.* **3**, 599-607 (2010).

263   2. Wang, K. & Bilek, S.L. Do subducting seamounts generate or stop large earthquakes?

264   *Geology* **39,** 819-822 (2011).

265   3. Shreve, R.L. & Cloos, M. Dynamics of sediment subduction, mélange formation, and

266   prism accretion. *J. Geophys. Res.* **91,** 10229-10245 (1986).

267   4. Bachmann, R. *et al.* Exposed plate interface in the European Alps reveals fabric

268   styles and gradients related to an ancient seismogenic coupling zone. *J. Geophys. Res.*

269   **114**, B05402, doi:10.1029/2008JB005927 (2009).

270   5. Fagereng, Å. & Sibson, R.H. Mélange rheology and seismic style. *Geology* **38,** 751-

271   754 (2010).

272   6. Rowe, C.D., Meneghini, F. & Moore, J.C. in *Geology of the Earthquake Source: A*

273   *Volume in Honour of Rick Sibson* (eds. Fagereng, Å., Toy, V.G. & Rowland, J.V.), 77-

274   95 (Geol. Soc. London, 2011).

275   7. Heuret, A., Lallemand, S., Funiciello, F., Pitomallo, C. & Faccenna, C. Physical

276   characteristics of subduction interface type seismogenic zones revisited. *Geochem.*

277   *Geophys. Geosyst*. **12**, Q01004, doi: 10.1029/2010GC003230 (2011).

278   8. Scholz, C.H. & Campos, J. The seismic coupling of subduction zones revisited. *J.*

279   *Geophys. Res*. **117,** B05310, doi:10.1029/2011JB009003 (2012).

280   9. Rubin, A.M., Gillard, D. & Got, J.-L. Streaks of microearthquakes along creeping

281   faults. *Nature* **400,** 635-641 (1999).

282   10. Hyndman, R.D., Yamano, M. & Oleskevich, D.A. The seismogenic zone of

283   subduction thrust faults. *Isl. Arc* **6,** 244-260 (1997).

284   11. Wallace, L.M. *et al*. Characterizing the seismogenic zone of a major plate boundary

285   subduction thrust: Hikurangi Margin, New Zealand. *Geochem. Geophys. Geosyst.* **10**,

286   Q10006, doi: 10.1029/2009GC002610 (2009).

287   12. Mochizuki, K., Yamada, T., Shinohara, M., Yamanaka, Y. & Kanazawa, T. Weak

288   interplate coupling by seamounts and repeating M ~ 7 earthquakes. *Science* **321**, 1194-

289   1197 (2008).

290   13. Power, W., Wallace, L.M., Wang, X. & Reyners, M. Tsunami hazard posed to New

291   Zealand by the Kermadec and Southern New Hebrides subduction margins: An

292   assessment based on plate boundary kinematics, interseismic coupling, and historical

293   seismicity. *Pure Appl. Geophys.* **169,** 1-36 (2012).

294   14. Hsu, Y.-J., Yu, S.-B., Song, T.-R. & Bacolcol, T. Plate coupling along the Manila

295   subduction zone between Taiwan and northern Luzon. *J. Asian Earth Sci.* **51,** 98-108

296   (2012).

297   15. Rowe, C.D., Moore, J.C., Remitti, F. & IODP Exp. 343/343T Scientists. The

298   thickness of subduction plate boundary faults from the seafloor into the seismogenic

299   zone. *Geology* **41**, 991-994 (2013).

300   16. Gratier, J.-P. *et al.* Aseismic sliding of active faults by pressure solution creep:

301   Evidence from the San Andreas Fault Observatory at Depth. *Geology* **39,** 1131-1134

302   (2011).

303   17. Richard, J., Gratier, J.P., Doan, M.-L., Boullier, A.-M. & Renard, F. Rock and

304   mineral transformations in a fault zone leading to permanent creep: Interactions

305   between brittle and viscous mechanisms in the San Andreas Fault. *J. Geophys. Res.* **119,**

306   8132-8153 (2014).

307   18. Gratier, J.-P., Guiguet, R., Renard, F., Jenatton, L. & Bernard, D. A pressure

308   solution creep law for quartz from indentation experiments. *J. Geophys. Res.* **114**,

309   B03403 (2009).

310   19. Schwarz, S. & Stöckhert, B. Pressure solution in siliciclastic HP-LT rocks –

311   constraints on the state of stress in deep levels of accretionary complexes.

312   *Tectonophysics* **255,** 203-209 (1996).

313   20. Kawabata, K., Tanaka, H. & Kimura, G. Mass transfer and pressure solution in

314   deformed shale of accretionary complex: examples from the Shimanto Belt, southwest

315   Japan. *J. Struct. Geol.* **29,** 697-711 (2007).

316   21. Fagereng, Å. in *Geology of the Earthquake Source: A Volume in Honour of Rick*

317   *Sibson* (eds. Fagereng, Å., Toy, V.G. & Rowland, J.V.), 55-76 (Geol. Soc. London,

318   2011).

319   22. Fagereng, Å. & Cooper, A.F. The metamorphic history of rocks buried, accreted and

320   exhumed in an accretionary prism: an example from the Otago Schist, New Zealand. *J.*

321   *Metamorph. Geol.* **28**, 935-954 (2010).

322   23. Bos, B. & Spiers, C. J. Frictional-viscous flow of phyllosilicate-bearing fault-rock:

323   microphysical model and implications for crustal strength profiles. *J. Geophys. Res.*

324   **107,** B2, 2028 (2002).

325   24. Niemeijer, A. & Spiers, C.J. in *High-Strain Zones: Structure and Physical*

326   *Properties* (eds. Bruhn, D. & Burlini, L.), 303-327 (Geol. Soc. London, 2005).

327   25. Den Hartog, S.A.M. & Spiers, C.J. A microphysical model for fault gouge friction

328   applied to subduction megathrusts. *J. Geophys. Res.* **119,** 1510-1529 (2014).

329   26. Molnar, P. & England, P. Temperatures, heat flux and frictional stress near major

330   thrust faults. *J. Geophys. Res.* **95,** 4833-4856 (1990).

331   27. Den Hartog, S.A.M., Saffer, D.M. & Spiers, C.J. The roles of quartz and water in

332   controlling unstable slip in phyllosilicate-rich megathrust fault gouges. *Earth Planets*

333   *Space* **66**, doi:1186/1880-5981-66-78 (2014).

334   28. Den Hartog, S.A.M., Niemeijer, A.R. & Spiers, C.J. Friction on subduction

335   megathrust faults: Beyond the illite-muscovite transition. *Earth Planet. Sci. Lett.* **373**, 8-

336   19 (2013).

337   29. Van Diggelen, E.W.E., De Bresser, J.H.P., Peach, C.J. & Spiers, C.J. High shear

338   strain behaviour of synthetic muscovite fault gouges under hydrothermal conditions. *J.*

339   *Struct. Geol.* **32**, 1685-1700 (2010).

340   30. Den Hartog, S.A.M. & Spiers, C.J. Influence of subduction zone conditions and

341   gouge composition on frictional slip stability of megathrust faults. *Tectonophysics* **600**,

342   75-90 (2013).

343   31. Niemeijer, A.R., Spiers, C.J. & Peach, C.J. Frictional behaviour of simulated quartz

344   fault gouges under hydrothermal conditions: Results from ultra-high strain rotary shear

345   experiments. *Tectonophysics* **460**, 288-303 (2008).

346   32. Dieterich, J. H. Modeling of rock friction: 1. Experimental results and constitutive

347   equations. *J. Geophys. Res.* **84**, 2161-2168 (1979).

348   33. Marone, C. Laboratory-derived friction laws and their application to seismic

349   faulting. *Annu. Rev. Earth Planet. Sci.* **26**, 643-696 (1998).

350   34. Scholz, C. H. Earthquakes and friction laws. *Nature* **391**, 37-42 (1998).

351   35. Syracuse, E.M., van Keken, P.E. & Abers, G.A. The global range of subduction

352   zone thermal models. *Phys. Earth. Planet. Inter.* **183**, 73-90 (2010).

353   36. Gao, X. & Wang, K. Strength of stick-slip and creeping subduction megathrusts

354   from heat flow observations. *Science* **345**, 1038-1041 (2014).

355   37. Tester, J.W., Worley, W.G., Robinson, B.A., Grigsby, C. & Feerer, J.L. Correlating

356   quartz dissolution kinetics in pure water from 25 to 625 ˚C. *Geochim. Cosmochim. Acta*

357   **58**, 2407-2420 (1994).

358   38 Hashimoto, Y., Nakaya, T., Ito, M. & Kimura, G. Tectonolithification of sandstone

359   prior to the onset of seismogenic subduction zone: Evidence from tectonic mélange of

360   the Shimanto Belt, Japan. *Geochem. Geophys. Geosyst.* **7**, Q06013 (2006).

361   39. Moore, J. C., Rowe, C. D. & Meneghini, F. in *The Seismogenic Zone of Subduction*

362   *Thrust Faults* (eds. Dixon, T. H. & Moore, J. C.), 288-315 (Colombia University Press,

363   2007).

364   40. Wallace, L. M. *et al.* Slow slip near the trench at the Hikurangi subduction zone,

365   New Zealand. *Science* **353**, 701-704 (2016).

366   41. Dragert, H., Wang, K. & James, T. A silent slip event on the deeper Cascadia

367   subduction interface. *Science* **292**, 1525-1528.

368   42. Obara, K., Hirose, H., Yamamizu, F. & Kasahara, K. Episodic slow slip events

369   accompanied by non-volcanic tremors in southwest Japan subduction zone. *Geophys.*

370   *Res. Lett.* **31**, L23602 (2004).

371   43. Liu, Y. & Rice, J. R. Aseismic slip transients emerge spontaneously in three-

372   dimensional rate and state modelling of subduction earthquake sequences. *J. Geophys.*

373   *Res.* **110,** B08307 (2005).

374   44. McCrory, P. A., Hyndman, R. D. & Blair, J. L. Relationship between the Cascadia

375   fore-arc mantle wedge, nonvolcanic tremor, and the downdip limit of seismogenic

376   rupture. *Geochem. Geophys. Geosyst.* **15**, 1071-1095 (2014).

377   45. Saffer, D. M. & Wallace, L. M. The frictional, hydrologic, metamorphic and thermal

378   habitat of shallow slow earthquakes. *Nat. Geosci.* **8**, 594-600 (2015).

379   46. Ruff, L. Do trench sediments affect great earthquake occurrence in subduction

380   zones? *Pure Appl. Geophys.* **129,** 263-282 (1989).

381   47. Wesnousky, S.G. Predicting the endpoints of earthquake ruptures. *Nature* **444,** 358-

382   360 (2006).

383   48. Fagereng, Å. Wedge geometry, mechanical strength, and interseismic coupling of

384   the Hikurangi subduction thrust, New Zealand. *Tectonophysics* **507**, 26-30 (2011).

385   49. Knipe, R. J. Deformation mechanisms – Recognition from natural tectonites. *J.*

386   *Struct. Geol.* **11**, 127-146 (1989).

387   50. Hicks, S. P. *et al.* The 2010 M_w 8.8 Maule, Chile earthquake: Nucleation and

388   rupture propagation controlled by a subducted topographic high. *Geophys. Res. Lett.* **39,**

389   L19308 (2012).

390

396   AUTHOR CONTRIBUTIONS: Both authors contributed to designing the study,

397   making the calculations, and writing the paper. Å.F. provided the microstructural

398   observations.

399   COMPETING INTERESTS: The authors declare that they have no competing financial

400   interests.

401   AUTHOR INFORMATION: Correspondence and requests for materials should be

402   addressed to Å. Fagereng (email: FagerengA@cardiff.ac.uk).

403   **Figure captions**

404   Figure 1: Example of pressure solution microstructures in a sample from the Chrystalls

405   Beach Complex, New Zealand.

406   **a,** Photograph of outcrop-scale mélange shear zone with sandstone lenses in cleaved

407   mudstone matrix. **b,** Photomicrograph (plane-polarised light) of sample from mélange

408   matrix, cleavage wraps around quartz clasts. **c,** Close-up of cleavage seams, rectangle

409   shows location of element maps of Si and Al; warm and cold colours show high and

410   low relative abundance, respectively. **d** Backscatter electron image of quartz clasts in

411   phyllosilicate matrix, accompanied by composite element map in **e**. **f,** Model

412   microstructure where matrix (grey) deforms by frictional sliding along foliations

413   (dashed lines), and clasts (black) deform by pressure solution[25]. All panels show dextral

414   sense of shear.

415   Figure 2: Strength curves calculated along a subduction thrust interface with properties

416   representative of the northern Hikurangi margin.

417   The pore fluid factor $\lambda = P_f/\sigma_v$, where P_f is pore fluid pressure and σ_v is vertical stress, is

418   moderate (0.8) in **a** and high (0.95) in **b**. The curves labelled 'microphysical model'

419   represent the strength of a fault where deformation occurs by slip on phyllosilicate

420   surfaces and pressure solution of intervening quartz. Microphysical model predictions

421   depend on grain size, D, and shear zone thickness, w, as shown in the legend, and

422   thermal profiles as shown in **c**, including initial thermal structure where the frictional

423   coefficient, μ, is 0.6. Supplementary Table S1 reports the full list of parameters.

424

425   Figure 3: Relations between slip velocity and frictional behaviour

426   **a,** Schematic relationship between friction coefficient and strain rate in the

427   microphysical model used here, indicating a change from velocity-strengthening to

428   velocity-weakening at high strain rate[25]. **b,** quantifies friction coefficient at a fixed

429   depth, as a function of strain rate or shear zone width at a fixed slip velocity, whereas **c**

430   combines calculations of friction coefficient vs. strain rate at all considered depths, to

431   depict the depth-dependent strain rates where a change from velocity-strengthening to

432   velocity-weakening is predicted (parameters as in Fig. 2).

433   Figure 4: Representations of the effect of frictional-viscous flow on megathrust seismic

434   style.

435   Subduction interfaces related to smooth (**a**) and rugged (**b**) topography on subducting

436   oceanic crust. Inferred transient and steady-state strain rate variations along these

437   interfaces are shown below, as is the inferred depth vs. creep strength profile as based

438   on Fig. 2 and down-dip variation in shear zone width.

439

Method

Element Maps

Element maps (Fig. 1c,d,e; Supplementary Figure 2) were plotted from energy

dispersive spectroscopy (EDS) data, which give relative abundance of elements,

measured on a carbon-coated, 30 μm thick sample. Maps in Fig. 1c were collected using

an electronprobe microanalyser at the University of Cape Town, with beam conditions

of 15 kV, 18.5 nA, 12 ms dwell time, and spot size of 1 μm. Electron backscatter

images in Fig. 1d, and map in Fig. 1e were acquired using a Zeiss Sigma HD scanning

electron microscope in the School of Earth & Ocean Sciences at Cardiff University. The

EDS data for these element maps were acquired with an beam accelerating voltage of 20

kV, nominal beam current of 4.7 nA, and a 20 ms dwell time. Resulting pixels are

approximately 1 μm.

Pressure-temperature estimates

To calculate the shear stress predicted by the microphysical model as a function of

depth, approximations of temperature, T, and effective normal stress, $\sigma_n{'}$, as functions

of depth are required. Because the subduction thrust interface is gently dipping, $\sigma_n{'}$ is

approximated as the effective vertical stress[51,52] so that

$$\sigma_n{'} = \rho g z (1 - \lambda) \qquad (1)$$

440

441

442

443

444

445

446

447

448

449

450

451

452

453

454

455

456

457

21

458   where ρ is the average density of overlying rock, taken as 2650 kg/m typical of

459   quartzofeldspathic rocks, g is gravitational acceleration, λ is pore fluid factor as defined

460   in the main text, and z is depth.

461   Temperature (in °C) is calculated according to the analytical derivation of Molnar

462   and England[26], as also applied to the Hikurangi margin by McCaffrey et al.[53], that sums

463   advective, radiogenic, and shear heating terms where

$$T = \frac{K_m}{SK_s}\frac{T_0 z}{\sqrt{\pi\kappa\left(t_0 + t_s\right)}} + \frac{A_r z^2}{2SK_s} + \frac{\tau V z}{SK_s} \qquad (2)$$

465   in which the dimensionless parameter S is defined as

$$S = 1 + b\frac{K_m}{K_s}\sqrt{\frac{Vz\sin\delta}{\kappa}} \qquad (3)$$

467   In these formulations, K_m and K_s are mantle and accretionary prism conductivities,

468   respectively, T_0 is temperature at the base of the lithosphere, κ is thermal diffusivity, t_0

469   is the age of the subducting oceanic crust at the trench, A_r is average radioactive heat

470   production rate in the forearc materials, τ is shear stress, and b is a geometrical factor. t_s

471   is the time to subduct the slab to depth z, approximated as $t_s = z/\left(V\sin\delta\right)$ where V is

472   slip velocity, assuming the megathrust accommodates the trench-normal component of

473   the plate convergence vector, and δ is the average dip angle of the subduction thrust

474   interface. Values for all the above parameters are listed in Supplementary Table 1. To

475   obtain the shear heating term in the initial thermal structure, τ is estimated as $\sigma_n{}'$

476   multiplied by a frictional coefficient of $\mu = 0.6$, estimating the lower end of the Byerlee

477   range[54]. After calculating shear stress according to the microphysical model, the

478   calculated shear stress as a function of depth is used to re-calculate the thermal

479   structure, which is then used to re-calculate shear stress. The change in thermal structure

480   from the first calculation to calculations involving shear stresses from the microphysical

481   model can be seen in Fig. 2c.

482   **Temperature-dependent mono-mineralic friction**

483   Values for the friction coefficient for phyllosilicates were determined assuming

484   the dominant phyllosilicate mineral to be illite and muscovite at temperatures below and

485   above 300 °C, respectively, and by assuming that temperature rather than effective

486   normal stress dominantly affects the friction coefficient. The friction coefficient of illite

487   as a function of temperature was determined by fitting a linear trend line to a

488   combination of the data by Tembe et al.[55] at 20°C and the data of Den Hartog et al.[27] at

489   200, 350 and 500°C, all representing final friction values (at 9.21 and ~40 mm shear

490   displacement, respectively) at a sliding velocity of 1 μm/s. Note that the sliding velocity

491   at ~40 mm shear displacement in the experiments of Den Hartog et al.[27] was 10 μm/s,

492   and we thus recalculated it to 1 μm/s using the value for $\Delta\mu/\Delta\ln V$, or $(a\text{-}b)$, for a

493   velocity step from 10 to 1 μm/s obtained in the same experiment. Similarly, the friction

494   coefficient of muscovite as a function of temperature was determined by fitting two

495   linear trendlines (joining at 600°C) to the data by Den Hartog et al.[28] at 200, 400 and

496   600°C and the data by Van Diggelen et al.[29] at 400, 500 and 700°C. These data

497   represent close to final friction coefficients, those by Den Hartog et al.[28] taken at a shear

498   strain of 50 and recalculated for 1 μm/s by the method described for illite and those by

499   Van Diggelen et al.[29] reported for the 0.5 μm/s step, which occurred at near steady state

500 friction. The resultant empirical function for phyllosilicate friction coefficient, μ_{ph},

501 becomes

502 $$\mu_{ph} \begin{cases} 0.320 + 9.10 \times 10^{-4}T, & T < 300\,°\text{C} \\ 0.300 + 6.18 \times 10^{-4}T, & 300\,°\text{C} \leq T < 600\,°\text{C} \\ 1.997 - 2.24 \times 10^{-3}T, & T \geq 600\,°\text{C} \end{cases}$$ (4)

503 This definition for the phyllosilicate friction coefficient was used to construct the

504 strength profiles for pure phyllosilicates and as input to the microphysical model.

505 The friction coefficient of quartz, for plotting the frictional strength of mono-

506 mineralic quartz aggregates in Fig. 2a,b, is estimated based on the room temperature

507 data of Tembe et al.[55], data at 140 °C of Den Hartog and Spiers[30] and the data at 400-

508 600 °C of Niemeijer et al.[31]. Based on similar arguments as for creating an empirical

509 function of phyllosilicate friction as a function of temperature, we obtain a function for

510 quartz friction, μ_{qtz}:

511 $$\mu_{qtz} \begin{cases} 0.750 - 1.04 \times 10^{-4}T, & T < 500\,°\text{C} \\ 1.41 - 1.43 \times 10^{-3}T, & T \geq 500\,°\text{C} \end{cases}$$ (5)

512 **Microphysical model by Den Hartog and Spiers[25]**

513 The microphysical model used to calculate the strength profiles (Fig. 2) was

514 derived by Den Hartog and Spiers[25]. The model describes the steady state frictional

515 behaviour of sheared illite-quartz mixtures, and assumes a matrix-supported shear zone

516 consisting of phyllosilicates and quartz clasts (Supplementary Figure 3). The quartz

517   clasts are uniformly distributed, arranged such that horizontal rows of clasts overlap. On

518   average, the phyllosilicates are aligned parallel to Y-shear bands, but locally

519   anastomose around the rigid clasts. Note that the Y-shear bands considered in the model

520   by Den Hartog and Spiers[25] will on average be parallel to the megathrust interface,

521   which implies that foliation that is parallel to these shear bands, described as

522   "horizontal" in the model, will be gently dipping in the megathrust setting.

523   Within the model microstructure, shear deformation occurs either within the "clast

524   body" zones containing a horizontal phyllosilicate foliation and quartz clasts (Type B

525   zones, Supplementary Figure 3) or in the "clast overlap" regions containing

526   anastomosing phyllosilicates and overlapping quartz clast edges (Type O zones,

527   Supplementary Figure 3). The horizontal foliation in the Type B zones abuts against the

528   quartz clasts, so that sliding on this foliation requires serial simple shear of the clast

529   "bodies". Shear of the clasts is assumed to occur by thermally activated deformation. By

530   contrast, in the Type O zones, the foliation anastomoses around the clast "overlaps". In

531   these zones, deformation can occur either by slip on the phyllosilicates at the zone

532   margins accommodated by shearing of the clast overlaps, or by slip on the curved

533   foliation accompanied by dilatation at extensional clast-matrix interface sites. Sliding on

534   the foliation is assumed to be a purely frictional process, which implies that slip on the

535   curved foliation will not occur unless a critical value of the macroscopic shear stress,

536   τ_{dil}, is attained. When slip is activated, it will cause dilatation and porosity development.

537   Den Hartog and Spiers[25] assumed that developing porosity concentrates at the

538   extensional quartz-illite interfaces (Supplementary Figure 3), resulting in a decrease in

539   the clast overlap distance, and hence in the mean inclination of the curved foliation.

540   This in turn causes a decrease in the rate of dilation per unit horizontal displacement on

541   the inclined foliation, i.e. a decrease in the dilatation angle ψ_{dil}, with increasing porosity.

542   Den Hartog and Spiers[25] assumed that the appearance of porosity, via clast/matrix

543   debonding, initiates compaction by thermally activated deformation of the clasts, which

544   accelerates as porosity increases. At steady state, dilation due to slip on the curved

545   foliation and compaction by the thermally activated mechanism must balance. This

546   competition between dilatation and compaction is of key importance since it will lead to

547   higher steady state porosities, a flatter foliation and lower frictional strength as sliding

548   velocity increases, and hence to velocity-weakening slip. This as opposed to non-

549   dilatant deformation, where the serial nature of deformation implies that the velocity-

550   dependence of friction is governed by thermally activated deformation of the quartz

551   clasts which is by definition velocity-strengthening. Dilatation, when active, is assumed

552   to continue until a limiting or critical state porosity is reached.

553   The model by Den Hartog and Spiers[25] does not strictly apply to muscovite.

554   However, in the absence of a microphysical model for the steady state frictional

555   behaviour of muscovite-quartz fault gouge, and since muscovite-quartz gouge shows

556   broadly similar behaviour to illite-quartz gouge[28], we have applied this model also at

557   temperatures >300°C where muscovite is expected to be the dominant phyllosilicate.

558   **Model calculations**

559   The reader is referred to Den Hartog and Spiers[25] for the derivation of the

560   equations governing the steady state frictional behaviour of the model microstructure

561   shown in Supplementary Figure 3 and described below.

562   Den Hartog and Spiers[25] derive their equations for the unit cell shown in

563   Supplementary Figure 3b, which has a horizontal dimension equal to horizontal clast

564   spacing:

565
$$L = \frac{k_f \pi D^2}{(D - x_0) f_{qtz}}$$
(6)

566   where k_f is a factor accounting for clast shape, D is grain size (clast diameter), f_{qtz}

567   is the volume fraction of quartz clasts, and x_0 is the vertical overlap of the clasts at zero

568   porosity defined by Den Hartog and Spiers[25] as

569
$$x_0 = D\left(1 - \sqrt{\frac{k_f \pi}{2 f_{qtz}}}\right)$$
(7)

570   As porosity, ϕ, increases due to dilatational slip on the curved foliation, this

571   overlap decreases from x_0 to an instantaneous value x according to the relation $x = (x_0 -$

572     $\phi D]/(1-\phi)$. The decrease in overlap in turn leads to a decrease in the width, d, of

573   overlapping clast segments (Supplementary Figure 3b), given $d = 2\sqrt{(Dx - x^2)}$.

574   During non-dilatant deformation at low slip velocities and/or high temperatures,

575   thermally activated shear deformation of the quartz clasts will be easy. The total

576   resistance to slip on the horizontal foliation will then be lower than the shear stress to

577   activate slip and dilatation on the anastomosing foliation. Under these conditions, Den

578   Hartog and Spiers[25] assumed that non-dilatant deformation takes place by the parallel

579   processes of (i) slip on the horizontal foliation with serial shear of the clast bodies in the

580   B zones of the microstructure plus (ii) slip on the horizontal phyllosilicates with serial

27

581 shear of clast overlaps at the margin of the O zones. Equilibrium between the shear

582 stresses supported by the B and O zones (τ_B and τ_O, respectively) requires $\tau_m = \tau_B = \tau_O$

583 where τ_m is the macroscopic shear stress. The shear stresses in the B and O zones were

584 derived by Den Hartog and Spiers[25]:

585
$$\tau_B = \tau_{ph}\left(1 - \frac{A_{qtz-b}}{LD}\right) + \tau_{qtz-b}\frac{A_{qtz-b}}{LD} \qquad (8)$$

586
$$\tau_O = \tau_{ph}\left(1 - \frac{A_{qtz-o}}{LD}\right) + \tau_{qtz-o}\frac{A_{qtz-o}}{LD} \qquad (9)$$

587 where τ_{ph} is the shear stress needed to drive frictional slip on the horizontal

588 phyllosilicate foliation and τ_{qtz-b} and τ_{qtz-o} are those needed to drive thermally activated

589 clast body and overlap deformation, respectively. A_{qtz-b} represents the average horizontal

590 area occupied by a single clast body within zone B of the unit cell, and is given $A_{qtz-b} =$

591 $[(\frac{1}{4}\pi D^2 - 2A'_{seg})D]/(D - 2x)$, where $A'_{seg} = [16x^2(D - x) + 3x^3]/[12\sqrt{(Dx - x^2)}]$ (Ref. 56)

592 is the area of an individual clast segment located in the overlap zone of the cell in the

593 plane of Supplementary Fig. 3 and $A_{qtz-o} = dD = 2D\sqrt{(Dx-x^2)}$ is the area over which the

594 overlap is displaced by slip at its base. Note that $\tau_{ph} = \mu_{ph}\sigma_n'$ where μ_{ph} is defined by

595 equation (4).

596 The parallel shear processes (i, ii) operating in the O and B zones mean that the

597 total, measured shear strain rate during non-dilatant deformation is $\dot{\gamma}_m = \dot{\gamma}_B + \dot{\gamma}_O$, where

598 $\dot{\gamma}_B$ and $\dot{\gamma}_O$ denote the shear strain rate contributed to the unit cell by each zone

599 respectively (i.e. $\dot{\gamma}_B$ and $\dot{\gamma}_O$ are determined by taking into account the thickness of the

600 B or O zone relative to the unit cell thickness). Note that the serial coupling of rate-

601   independent slip on the phyllosilicates with thermally activated deformation of clasts

602   implies that $\dot{\gamma}_B = \dot{\gamma}_{qtz-b}$ and $\dot{\gamma}_O = \dot{\gamma}_{qtz-o}$, where, $\dot{\gamma}_{qtz-b}$ and $\dot{\gamma}_{qtz-o}$ are the shear strain

603   rate contributions to the unit cell due to thermally activated deformation of the clast

604   bodies and clast overlaps, respectively. Thermally activated deformation was assumed

605   to occur via pressure solution by Den Hartog and Spiers[25], yielding:

606
$$\dot{\gamma}_{qtz-b} = \frac{AI\tau_{qtz-b}\Omega}{RT} \frac{D-2x}{D(D-x)} \qquad (10)$$

607
$$\dot{\gamma}_{qtz-o} = \frac{2I\tau_{qtz-o}\Omega}{RT} \frac{1}{\sqrt{Dx-x^2}} \qquad (11)$$

608   Where A is a shape factor, I is the product of the dissolution rate coefficient k_+

609   and molar volume Ω of quartz, and R is the gas constant.

610   Following Den Hartog and Spiers[25], we obtained τ_m as a function of $\dot{\gamma}_m$, by first

611   imposing $\dot{\gamma}_m$, defined as $\dot{\gamma}_m = V/w$ where w is the shear zone width. We next solved

612    $\dot{\gamma}_m = \dot{\gamma}_B + \dot{\gamma}_O$ together with $\tau_m = \tau_B = \tau_O$ to obtain $\dot{\gamma}_B$ or $\dot{\gamma}_{qtz-b}$. We subsequently used

613    $\dot{\gamma}_{qtz-b}$ to determine τ_{qtz-b} via equation (10). The value of τ_{qtz-b} obtained, then yielded τ_B

614    $= \tau_m$ through equation (8). Note that in the current calculations we prevented $\dot{\gamma}_O$ from

615   taking a negative value in the non-dilatant regime[57].

616   At high slip rates or low temperatures, thermally activated shear deformation of

617   the quartz clasts is difficult, leading to an increase in the total resistance to shear on the

618   horizontal foliation. In the model microstructure of Den Hartog and Spiers[25] this would

619   ultimately activate slip on the curved phyllosilicates in the overlap (O) zones of the

620   microstructure. The measured shear strength in that case is equal to that required to

621   activate slip on the anastomosing foliation, τ_{dil}, derived by Den Hartog and Spiers[25] to

622   be

623
$$\tau_{dil} = \left\{ \frac{\mu_{ph}\left(1 + \tan^2 \Psi_{fr}\right)}{1 - \mu_{ph}^2 \tan^2 \Psi_{fr}} \right\} \sigma_n' \tag{12}$$

624   where $\tan \Psi_{fr}$ is a straight line approximation of the curved foliation, i.e.

625
$$\tan \Psi_{fr} = \frac{2\left(D - x_0\right)f_{qtz}}{k_f \pi D^2} x \tag{13}$$

626   Stress equilibrium between B and O zones means that in the dilatant case $\tau_m = \tau_{dil}$

627    $= \tau_B = \tau_O$. The total shear strain rate $\dot{\gamma}_m$, in turn, is given $\dot{\gamma}_m = \dot{\gamma}_B + \dot{\gamma}_O + \dot{\gamma}_{dil}$, or

628   equivalently $\dot{\gamma}_m = \dot{\gamma}_{qtz-b} + \dot{\gamma}_{qtz-o} + \dot{\gamma}_{dil}$, where $\dot{\gamma}_{dil}$ is the shear strain rate contribution to

629   the unit cell by dilatant slip on the curved phyllosilicates. This mechanism produces an

630   associated dilational strain rate, $\dot{\varepsilon}_{dil}$, which Den Hartog and Spiers[25] defined following

631   the classical soil mechanics approach to granular flow, i.e.

632
$$\dot{\varepsilon}_{dil} = \left(\frac{d\varepsilon_{dil}}{d\gamma_{dil}}\right)\frac{d\gamma_{dil}}{dt} = \left(\tan \Psi_{dil}\right)\dot{\gamma}_{dil} \tag{14}$$

633   Den Hartog and Spiers[25] defined the dilatation angle Ψ_{dil} as the steepest portion of

634   the curved, i.e. sinusoidal, foliation:

635
$$\tan \Psi_{dil} = \sqrt{\frac{\pi f_{qtz}}{2k_f} - \frac{\pi}{2(1-\phi)}}$$
(15)

636 This angle (Ψ_{dil}) decreases with increasing porosity, reaching zero at a limiting or

637 "critical state" porosity, defined $\phi_c = x_0/D$ when $x = 0$.

638 The porosity generated by dilatant slip will induce compaction by thermally

639 activated deformation of the quartz clasts at a rate $\dot{\varepsilon}_{comp}$. Taking compaction as positive,

640 the total, measured compaction strain rate is therefore given $\dot{\varepsilon}_m = \dot{\varepsilon}_{comp} - \dot{\varepsilon}_{dil}$. At

641 steady state, dilatation and compaction must balance, resulting in a steady state porosity

642 corresponding to the condition that $\dot{\varepsilon}_m = 0$ or $\dot{\varepsilon}_{comp} = \dot{\varepsilon}_{dil}$. Following Den Hartog and

643 Spiers[25], $\dot{\varepsilon}_{comp}$ is given by:

644
$$\dot{\varepsilon}_{comp} = \frac{2I\sigma'_n\Omega}{RT} \frac{A_{pore}}{(D-x)DL}$$
(16)

645 Compaction occurs by pressure solution transfer from compressively stressed

646 illite-quartz interfaces to debonded (dilated) interfaces (pore walls) with surface area

647 A_{pore}, written $A_{pore} = (A_{pore-c}/2)(\phi/\phi_c)^n$ where ϕ_c and A_{pore-c} are the porosity and pore area

648 per clast at the critical state. Den Hartog and Spiers[25] derived that $A_{pore-c} = (\pi D^2)/2$.

649 To calculate τ_m as a function of $\dot{\gamma}_m$ in the dilatant regime, we followed the

650 procedure by Den Hartog and Spiers[25] and incremented the porosity from 0 to ϕ_c and

651 calculated the corresponding values of $\tan \Psi_{dil}$ and $\tan \Psi_{fr}$ using equations (15) and (13).

652 Using $\tan \Psi_{fr}$, equation (12) gives τ_{dil}. The corresponding shear strain rate $\dot{\gamma}_m$ is

653 calculated via $\dot{\gamma}_m = \dot{\gamma}_{qtz-b} + \dot{\gamma}_{qtz-o} + \dot{\gamma}_{dil}$ and using the flow laws in equations (10) and

654 (11). Here, $\dot{\gamma}_{dil}$ is obtained via equation (14) and using the steady state condition

655 $\dot{\varepsilon}_{comp} = \dot{\varepsilon}_{dil}$, where $\dot{\varepsilon}_{comp}$ is calculated using equation (16).

656 In our calculations, we assumed cylindrical quartz clasts ($k_f = 0.25$) of either 10 or

657 100 μm in diameter, taking up a volume fraction of 0.45. Following Den Hartog and

658 Spiers[25], we assume that pressure solution is controlled by the interfacial reactions of

659 dissolution and precipitation and can be described using the empirical equation for the

660 dissolution rate coefficient provided by Tester et al.[37]:

661 $$k_+ = 276 \exp\left(\frac{-90100}{RT}\right) \qquad\qquad (17)$$

662 with T in Kelvin. We used a shape factor A of π in our calculation of the clast body

663 shear strain rate, while a factor of 2 was used in the original model. We also follow the

664 assumption that the porosity can be characterised by an exponent n of 0.3 (Ref. *25*).

665 To determine our shear strength versus depth profiles predicted by the

666 microphysical model, we selected σ_n', T and the corresponding μ_{ph} at each depth. Using

667 this input, we obtained τ_m as a function of $\dot{\gamma}_m$ (incorporating both non-dilatant and

668 dilatant deformation) following the above procedure. We next used the assumed

669 subduction velocity of 40 mm/yr and shear zone thickness (1 to 100 m in the current

670 calculations) to select relevant $\dot{\gamma}_m$ and determined τ_m at that shear strain rate.

671 The result of our calculations, shown in Fig. 2, yield dilatant deformation at

672 shallow depths and low temperatures for the shear strain rates explored in this study.

673   With increasing depth and temperature shear deformation of the quartz clasts by

674   pressure solution becomes easier, resulting in a transition to non-dilatant deformation.

675   To illustrate this effect, we show the calculated values of τ_{ph}, $\tau_{qtz\text{-}b}$ (for non-dilatant

676   shear), and the inferred shear stress as a function of depth, for the scenario where D is

677   100 μm, w is 100 m, and λ is 0.95, in Supplementary Figure 4. For any given set of

678   conditions, the transition to non-dilatant deformation depends on strain rate, and we plot

679   the strain rate at which the transition occurs, as a function of depth, in Fig. 3c.

680   **Code and data availability**

681   Code and additional data are available from the authors on request.

682   **Additional References**

683   51. Lamb, S. Shear stresses on megathrusts: Implications for mountain building behind

684   subduction zones. *J. Geophys. Res.* **111**, B07401, doi:10.1029/2005JB003916 (2006).

685   52. Wada, I., Wang, K., He, J. & Hyndman, R.D. Weakening of the subduction interface

686   and its effects on surface heat flow, slab dehydration, and mantle wedge

687   serpentinization. *J. Geophys. Res.* **113**, B04402, doi:10.1029/2007JB005190 (2008).

688   53. McCaffrey, R., Wallace, L.M. & Beavan, J. Slow slip and frictional transition at low

689   temperature at the Hikurangi subduction zone. *Nat. Geosci.* **1**, 316-320 (2008).

690   54. Byerlee, J. D. Friction of rocks. *Pure Appl. Geophys.* **116**, 615-626 (1978).

691   55. Tembe, S., Lockner, D.A. & Wong, T.-F. Effect of clay content and mineralogy on

692   frictional sliding behaviour of simulated gouges: Binary and ternary mixtures of quartz,
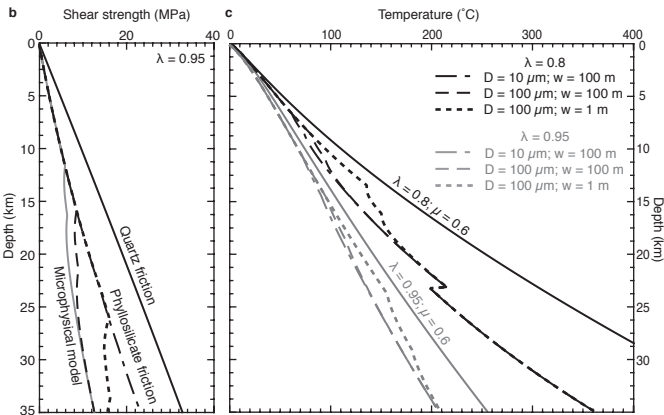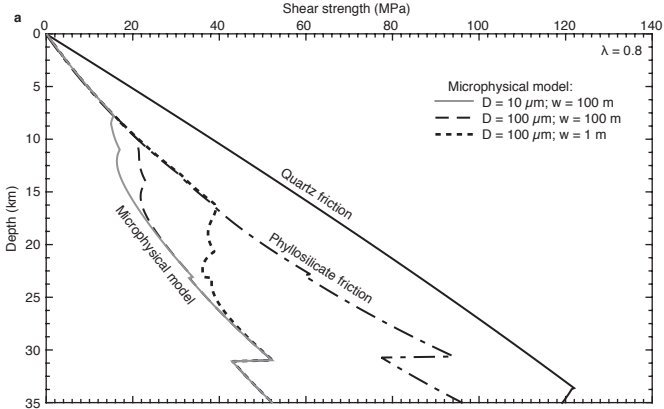
693   illite and montmorillonite. *J. Geophys. Res.* **115**, B03416, doi:10.1029/2009JB006383
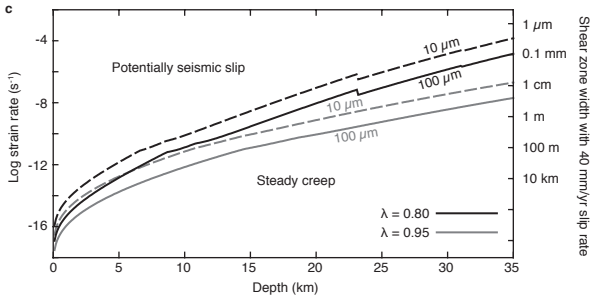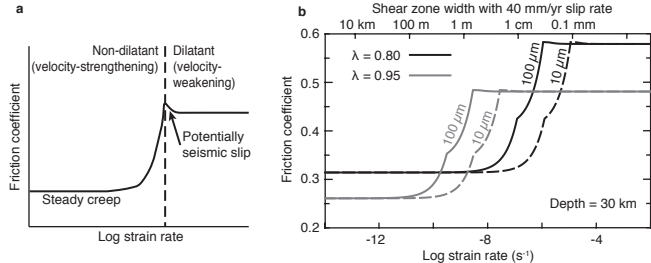
694   (2010).

695   56. Harris, J.W. & Stocker, H. *Handbook of Mathematics and Computational Science.*
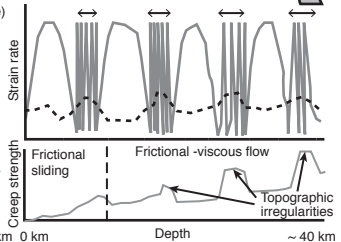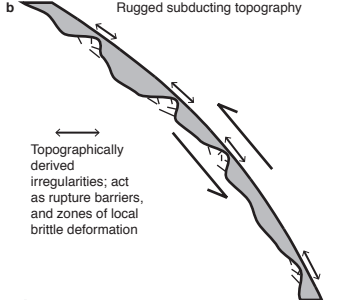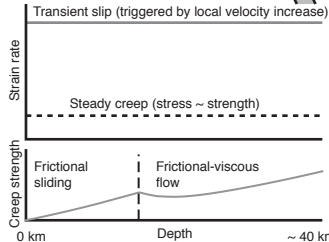
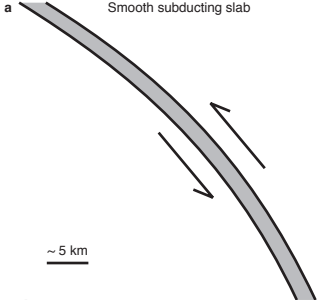696   (Springer-Verlag, New York, 1998).

697   57. Noda, H. Implementation into earthquake sequence simulations of a rate- and state-

698   dependent friction law incorporating pressure solution creep. *Geophys. J. Int.* **205**,

699   1108-1125 (2016).

700

Curved phyllosilicate foliation: slip + dilatation or horizontal displacement of clast extremities

Horizontal phyllosilicate foliation: non-dilatant deformation + "flow" of quartz

Porosity at dilatant interfaces

Unit cell

Quartz clast

Si
Al
K
Ti

a Friction coefficient vs. Log strain rate

Non-dilatant (velocity-strengthening) | Dilatant (velocity-weakening)

Potentially seismic slip

Steady creep

b Shear zone width with 40 mm/yr slip rate

10 km   100 m   1 m   1 cm   0.1 mm

λ = 0.80
λ = 0.95

100 μm
10 μm

Friction coefficient vs. Log strain rate (s⁻¹)

Depth = 30 km

c Log strain rate (s⁻¹) vs. Depth (km)

Potentially seismic slip

10 μm
100 μm

Steady creep

10 μm
100 μm

λ = 0.80
λ = 0.95

Shear zone width with 40 mm/yr slip rate

1 μm   0.1 mm   1 cm   1 m   100 m   10 km

a   Smooth subducting slab

b   Rugged subducting topography

~ 5 km

Topographically derived irregularities; act as rupture barriers, and zones of local brittle deformation

Transient slip (triggered by local velocity increase)

Strain rate

Steady creep (stress ~ strength)

Strain rate

Creep strength

Frictional sliding

Frictional-viscous flow

0 km   Depth   ~ 40 km

Creep strength

Frictional sliding

Frictional -viscous flow

Topographic irregularities

0 km   Depth   ~ 40 km

Subduction megathrust creep governed by pressure solution and frictional-viscous flow

Åke Fagereng and Sabine A.M. den Hartog
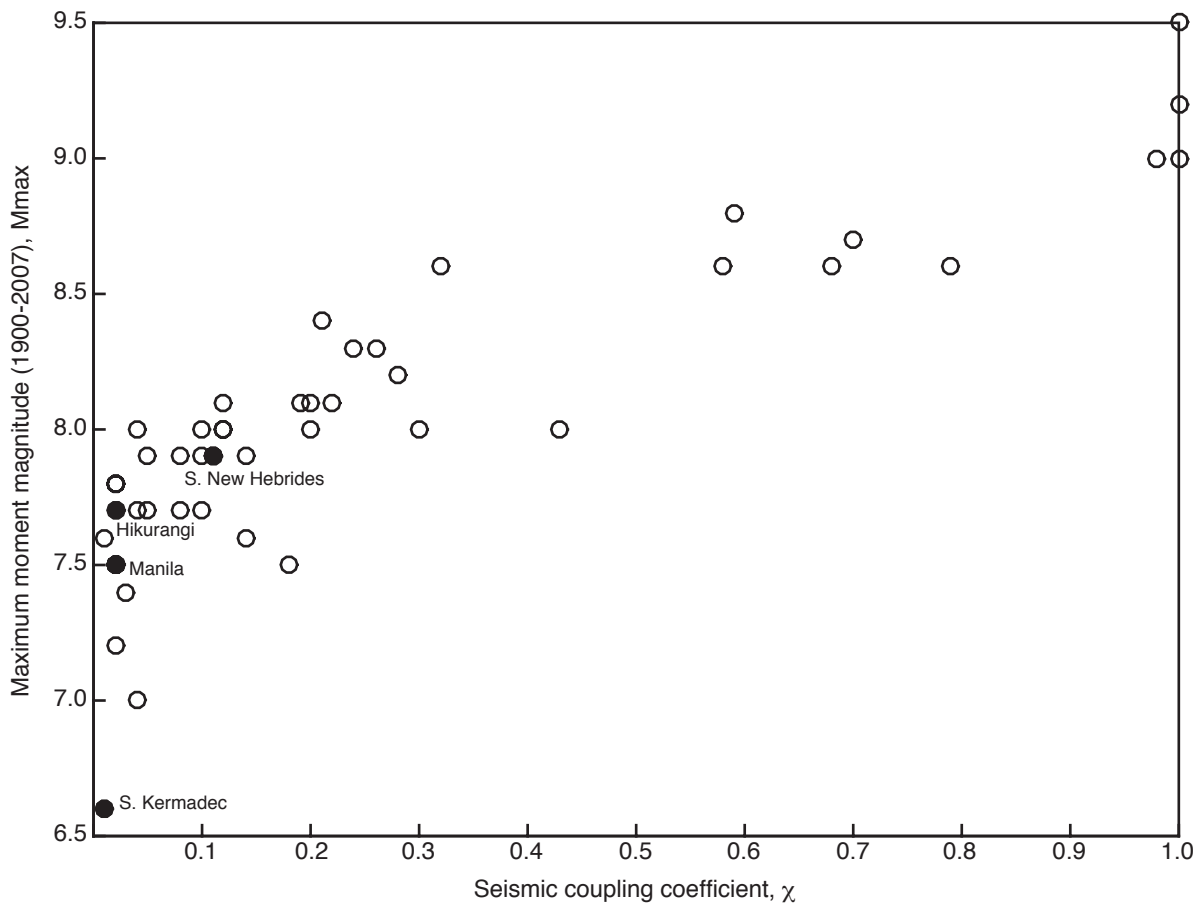
Supplementary Figure S1: Plot of maximum moment magnitude, *Mmax*, against seismic coupling coefficient, χ. The data are from the compilation of Heuret et al. (2011), but limiting the maximum seismic coupling coefficient to 1.0. Examples in the main text are highlighted in solid circles. Note that Hikurangi in this plot includes both northern and southern Hikurangi, and that the $M_w7.7$ event in the Heuret et al. (2011) compilation may have included significant slip on a splay fault in the overlying accretionary prism (Wallace et al., 2009). Thus, both the coupling coefficient and the maximum magnitude may be overestimated. The southern Japan Trench is not highlighted despite being mentioned in the main text, as the area referred to is relatively small, but described in detail by Mochizuki et al. (2008); it is not added to retain consistency in the plotted data.

Data in Fig. S1 were compiled by Heuret et al. (2011) using data from the Harvard CMT catalogue for $M_w \geq 5.5$ earthquakes from the 1976-2007 time period, including 1900-1975 for $M_w \geq 7.0$ events in the Centennial catalogue of (Engdahl and Villasenor, 2002). Earthquake locations were, if possible, relocated from the EHB catalogue of Engdahl et al. (1998). Thus, Heuret et al. (2011) extracted earthquakes with locations and, if available, nodal planes that align with the subduction thrust interface. From this data set, they defined the seismogenic zone of a number of megathrust interfaces, 49 for which they provide both *Mmax* and χ.

For the 49 subduction interfaces plotted in Fig. S1, *Mmax* is the largest subduction thrust earthquake identified in the Heuret et al. (2011) compilation, i.e. that occurred between 1900 and 2007, and fell on the inferred megathrust interface. We note that overestimates may occur, through inclusion of poorly located events, that were not actually megathrust events, particularly events prior to 1964 that were not relocated in the EHB catalogue.

To calculate χ, the amount of seismic slip and the rate of plate convergence must be estimated for each region. Defining seismic moment of a single earthquake as $M_0 = GLWu$, where G is shear modulus (50 GPa), L and W are the length and width of the rupture area, and u is average slip, the seismic slip rate for a time period T is $v_s = Su/T = SM_0/(GLWT)$ (Brune, 1968). The seismic coupling coefficient, χ, can be defined as the ratio of v_s to the subduction velocity as defined by global plate kinematic models, and was calculated accordingly by Heuret et al. (2011).

References

Brune, J.N. Seismic moment, seismicity, and rate of slip along major fault zones. *J. Geophys. Res.* **73**, 777-784 (1968).

Engdahl, R. & Villaseñor, A. Global seismicity: 1900-1999, in *International Handbook of Earthquake and Engineering Seismology, Part A* (eds Lee, W.H.K. *et al.*) 665-690 (Academic, Amsterdam, 2002).

Engdahl, R., Van Der Hilst, R. & Buland, R. Global teleseismic earthquake relocation with improved travel times and procedures for depth determination. *Bull. Seismol. Soc. Am.* **88**, 722-743 (1998).

Heuret, A., Lallemand, S., Funiciello, F., Pitomallo, C. & Faccenna, C. Physical characteristics of subduction interface type seismogenic zones revisited. *Geochem. Geophys. Geosyst.* **12**, Q01004, doi: 10.1029/2010GC003230 (2011).

Mochizuki, K., Yamada, T., Shinohara, M., Yamanaka, Y. & Kanazawa, T. Weak interplate coupling by seamounts and repeating M ~ 7 earthquakes. *Science* **321**, 1194-1197.

Wallace, L.M. *et al.* Characterising the seismogenic zone of a major plate boundary subduction thrust: the Hikurangi Margin, New Zealand. *Geochem. Geophys. Geosyst.* **10**, Q10006, doi:10.1029/2009GC002610 (2009).
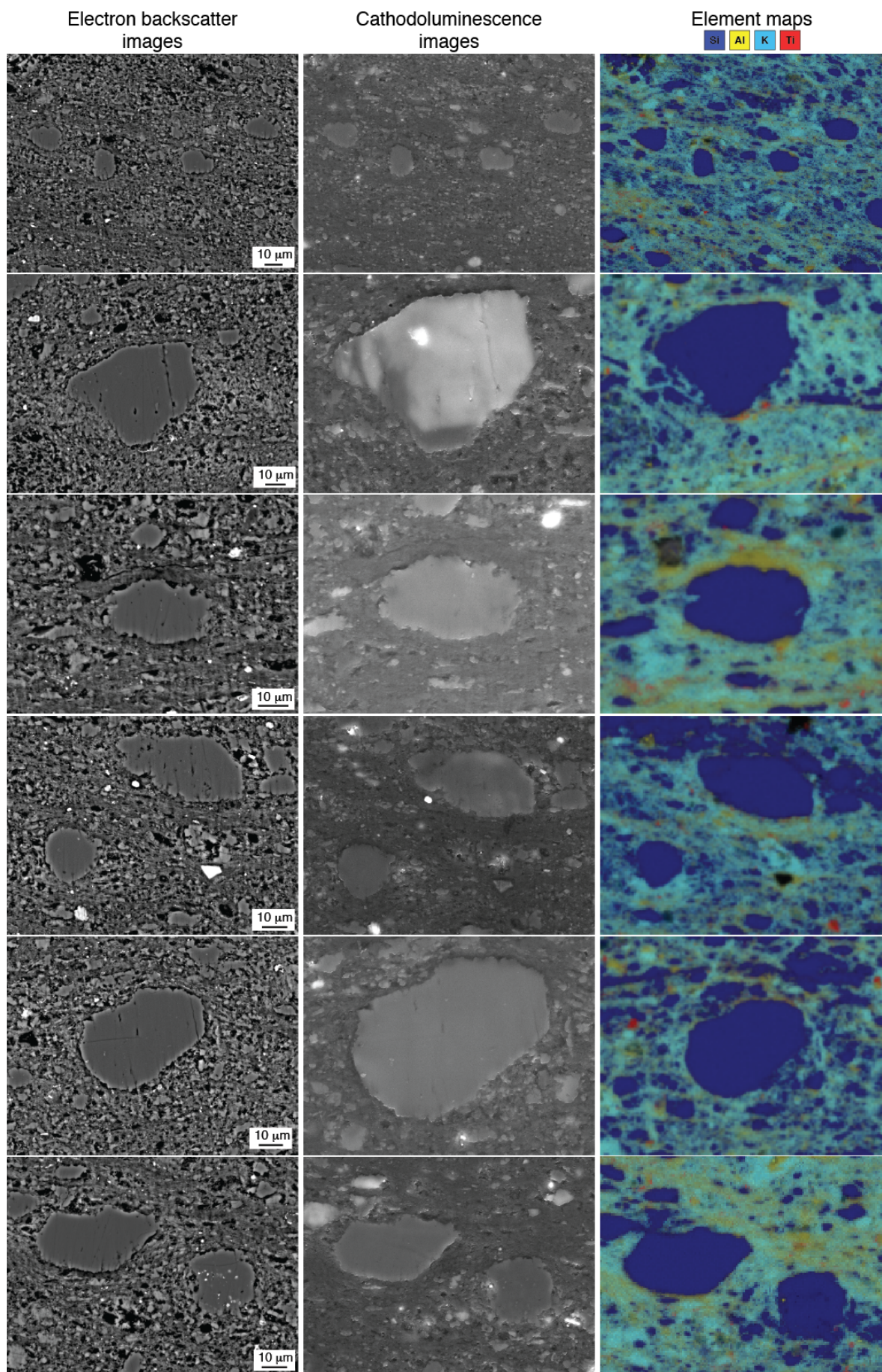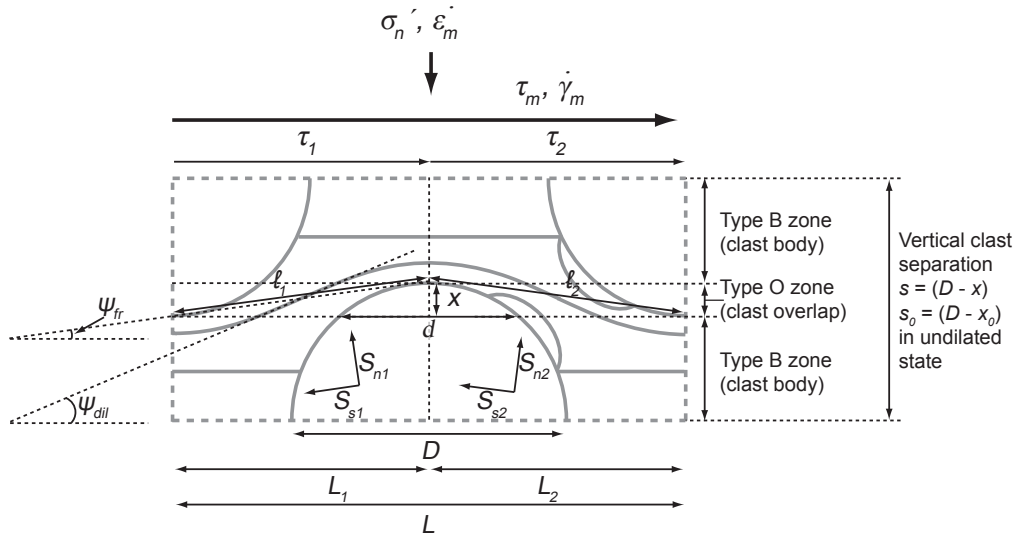
Supplementary Figure S2: Scanning electron microscope images of Chrystalls Beach sample. Minor pore space development in pressure shadows can be seen in BSE images in the left column, and silica enrichment in pressure shadows can be discerned from EDS maps in the right column. The middle column shows little CL variation within most quartz clasts.
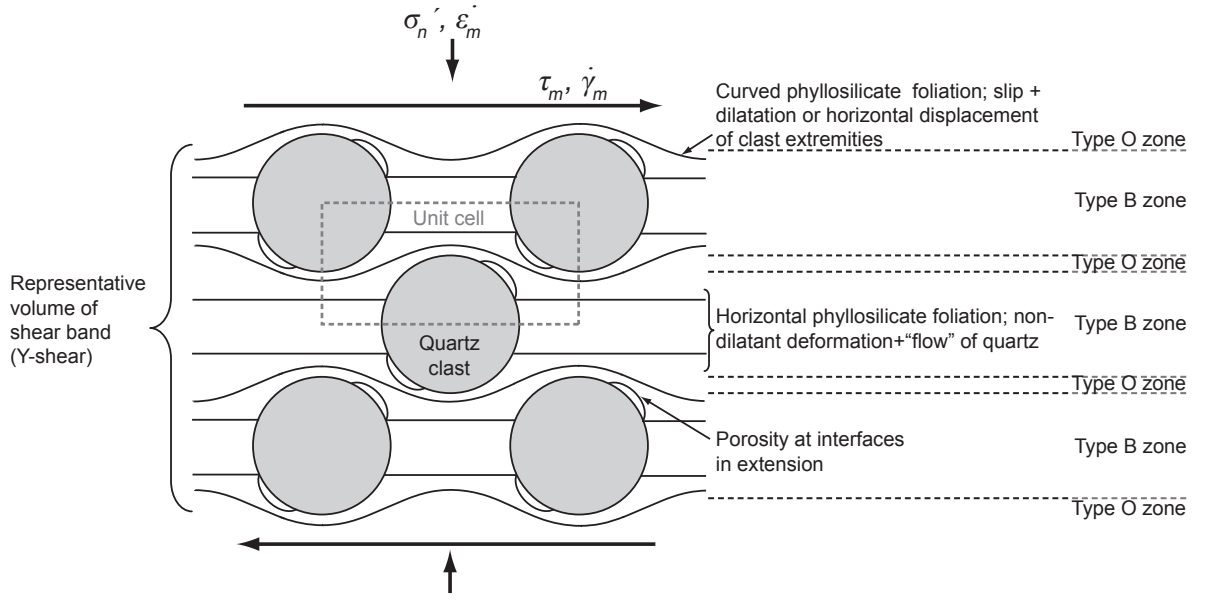
Supplementary Figure S3: Model microstructure assumed for phyllosilicate-quartz gouge undergoing shear deformation. **a**. Shows the representative microstructure, and the definition of clast body zones (B), clast overlap zones (O), and the unit cell as referred to in the method, and originally defined by Den Hartog and Spiers (2014, *25* in main text). In this figure, σ_n' is the effective normal stress, τ_m is the macroscopic shear stress, $\dot{\gamma}_m$ is the macroscopic or imposed shear strain rate and $\dot{\varepsilon}_m$ is the macroscopic rate of compaction. **b.** Shows the definition of the microstructural variables; the key variables are referred to and defined in the Methods. Note that the curved foliation is drawn with an exaggerated amplitude for clarity. Figure taken from Den Hartog and Spiers (2014, Ref *25* in the main text).
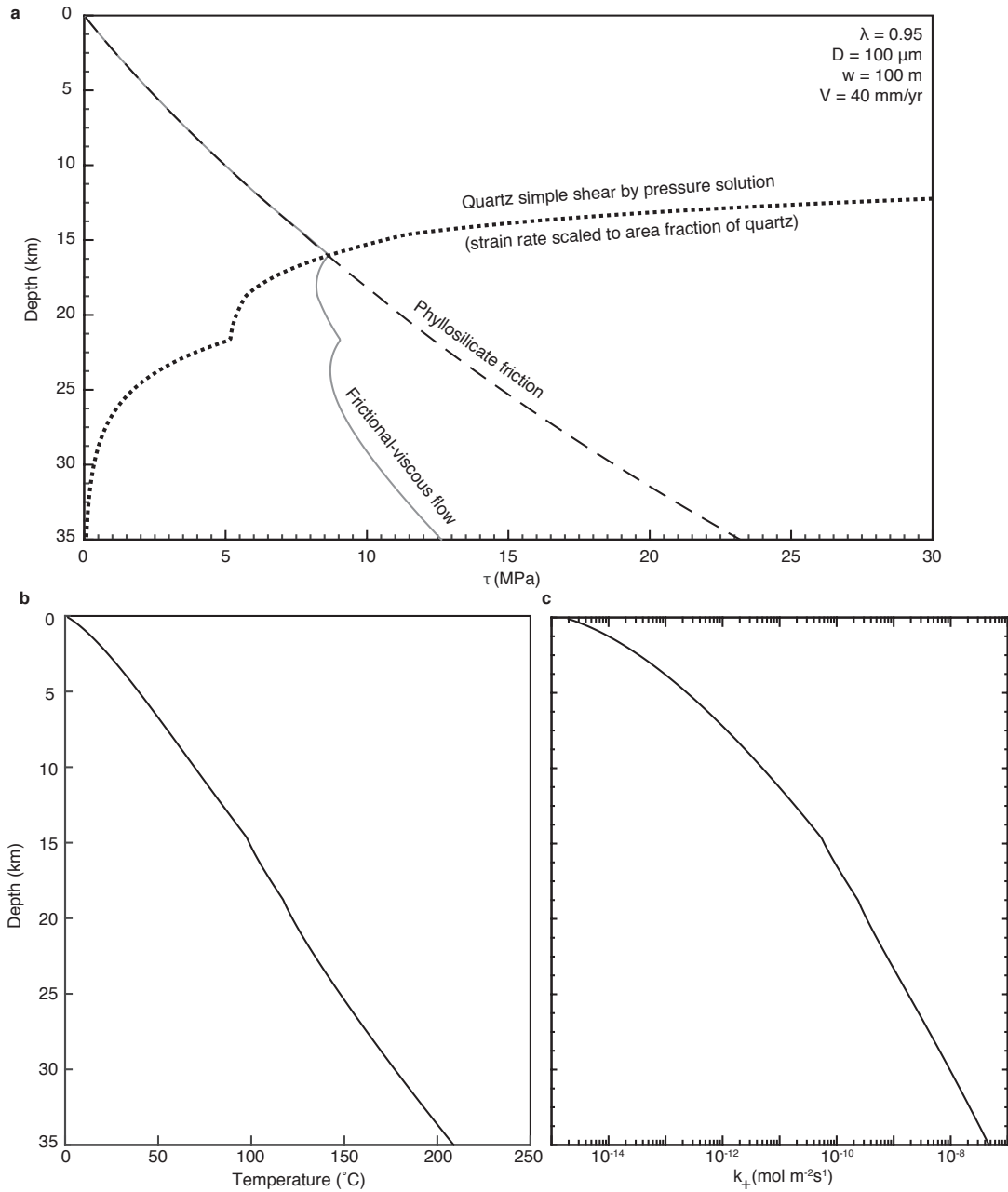
Supplementary Figure S4: Figure showing details of calculated parameters, for the scenario where quartz clast size, D, is 100 µm, shear zone width, w, is 100 m, and the pore fluid factor, λ, is 0.95. **a.** calculated values of phyllosilicate frictional resistance, τ_{ph}, shear stress required for simple shear of quartz clast bodies, $\tau_{qtz\text{-}b}$ (for non-dilatant shear), and the inferred shear stress for frictional-viscous flow at the given strain rate of $v/w = 1.3 \times 10^{-11}$ s^{-1}, as a function of depth. **b.** Temperature as a function of depth. **c.** Dissolution rate constant for quartz in water, k_+, as a function of depth.

Supplementary Table S1 List of parameter values used in the calculations performed in this paper.

Parameter	Meaning	Value
Temperature and stress		
A_r	Average radiogenic heat production in the forearc	10^{-6} W m^{-3}
b	Geometric constant	1.0
K_m	Mantle conductivity	3.3 W m^{-1} K^{-1}
K_s	Accretionary prism conductivity	2.55 W m^{-1} K^{-1}
t_0	Age of subducting oceanic crust at the trench	80 Ma
T_0	Temperature at the base of the lithosphere	1300 ˚C
V	Average fault slip rate	40 mm yr^{-1}
δ	Average dip of subduction thrust interface	15°
λ	Pore fluid factor	0.8 or 0.95
κ	Thermal diffusivity	10^{-6}
ρ	Average density above the shear zone	2650 kg m^{-3}
Microphysical model		
A	Shape factor in the clast body shear strain rate equation	π
D	Clast diameter (grain size)	10 or 100 μm
f_{qtz}	Volume fraction of quartz	0.45
k_f	Constant depending on the 3-D clast shape, ¼ for cylinder	0.25
k_+	Dissolution rate coefficient	$= 276 \times \exp(-90100/[R \times T\,(\text{K})])$ mol m^{-2} s^{-1}
n	Exponent in relation describing pore area, pore shape evolution parameter	0.3
R	Universal gas constant	8.31462 J mol^{-1} K^{-1}
w	Average shear zone thickness	1 - 100 m
μ_{ph}	Friction coefficient within phyllosilicates	0-300°C: $= 0.3199 + 9.101 \times 10^{-4}\,T\,(\text{°C})$ 300-600°C: $= 0.2997 + 6.180 \times 10^{-4}\,T\,(\text{°C})$ 600-700°C: $= 1.9967 - 2.244 \times 10^{-3}\,T\,(\text{°C})$
Ω	Molar volume of quartz	2.27×10^{-5} m^3 mol^{-1}